Analysis of the laterally bent piezoelectric semiconductor fibers with variable cross-sections

Zelin Xu,[1] Kai Fang,[1] Mengran Yu,[1] Tiqing Wang,[1] Peng Li,[1] Zhenghua Qian,[1, a)] and Dianzi Liu[2]
[1)] *State Key Laboratory of Mechanics and Control of Mechanical Structures, College of Aerospace Engineering, Nanjing University of Aeronautics and Astronautics, Nanjing, China*
[2)] *School of Engineering, University of East Anglia, Norwich NR4 7TJ, U.K.*

(Dated: March 29, 2023)

Piezoelectric semiconductor materials (PS) have attracted much attention in recent years due to their unique properties. This paper explores the electromechanical coupling behavior of bent piezoelectric semiconductor fibers with non-uniform cross-sectional areas. The study uses the generalized differential quadrature method (GDQM) to numerically solve the field equations with variable coefficients derived from piezoelectric theory. The research examines the mechanical and electrical field distribution of bent variable cross-section fibers, comparing the performances of non-uniform fibers with different profiles. The study reveals that the variable cross-section profile of the fiber changes the characteristic of the uniform fiber's electrical distribution along the axis, and it exhibits a more sensitive and stronger electrical response to the same external force. The research also shows that the concavity and convexity of the radius distribution function of the non-uniform fibers determine whether there are extreme points of surface potential. Finally, the study suggests that by designing extreme points of the PS fiber profile, surface potential extreme points can be artificially created at the same location. These results offer a theoretical direction for creating advanced piezoelectric semiconductor nanodevices and present novel insights into designing higher-efficiency nanogenerators and mechanical strain sensors in the future.

I. INTRODUCTION

Piezoelectric semiconductor (PS) innovative nanostructures have proliferated in the last few decades. They have been successfully used in the fields of nanogenerators[1,2], piezotronic field-effect transistors[3,4], piezotronic and chemical sensors[5,6], piezotronic logic nanodevices[7], piezotronic acoustic tweezers[8] and others. Among the various PS structures, one-dimensional fibers have attracted the most interest among scholars. Compared to other structures such as thin films and tubes, PS fibers can be fabricated more easily and can withstand larger mechanical deformation[9]. Consequently, their electromechanical behaviors, including vibration[10,11], bending[12], extension[13,14], and torsion[15], have been extensively investigated, and the results have proven invaluable for device design.

It is noteworthy that the above-mentioned studies are all based on uniform PS fibers. However, some recent studies suggest that non-uniform fibers with variable cross-sections may exhibit better piezotronic performance. For instance, Hu et al.[16] proposed a simple, cost-effective, and robust approach for fabricating a nanogenerator by dispersing conical ZnO nanofibers on a flat polymer film. They found that the output power was strong enough to drive a commercial liquid crystal display continuously. Using the finite element method, Araneo et al. simulated the axial[17] and transverse[18] deformation of tapered PS nanofibers and demonstrated that non-uniform strain leads to higher on-off ratios of devices. Fang et al.[19] investigated the electromechanical properties of extensional non-uniform PS fibers using a macroscopic phenomenological theory. They proposed a power series expansion method to solve the differential equations with variable coefficients describing the field distributions and demonstrated that non-uniform fibers are more sensitive to external forces. Ren[20] and his team derived theoretical approximate closed-form solutions for the electromechanical fields in strain gradient non-uniform PS fibers, which is an extension of the general PS theory. Nonetheless, studies on non-uniform PS fibers are still rare. More importantly, as material science continues to develop, it will become increasingly feasible to perform precise designs of PS fiber configurations, requiring a deeper understanding of the properties of non-uniform PS fibers. The differences in the mechanical and electrical properties of variable cross-section fibers and uniform fibers also result in some peculiar phenomena under bending deformation. For example, in the case of a monotonous change in cross-sectional area, the surface potential does not always correspondingly change monotonically, but instead sometimes exhibits extreme points. Another example is that when an extreme point appears in the cross-sectional area, the coordinates of the corresponding shear stress extreme point exhibit an offset relative to the area extreme point. These phenomena are obtained through current finite element simulations, but lack a reasonable theoretical explanation, which is the starting point of this paper. Our research aims to fill the gap in the theoretical derivation of the bending deformation of variable cross-section fibers and provide a reliable and effective theoretical solution. Additionally, the obtained theory will be used to analyze and explain the above-mentioned mechanical and electrical behavior.

This paper focuses on the study of non-uniform PS fibers in bending. The analysis is based on the general macroscopic theory, which includes the piezoelectricity theory and the drift-diffusion theory of carriers. The generalized differential quadrature method (GDQM) is adopted to numerically solve the coupled equations with variable coefficients. Following that, the electromechanical responses of the fibers un-

---

[a)] **Corresponding Author**; Electronic mail: qianzh@nuaa.edu.cn

der different contour profiles and external forces are then comprehensively investigated. The article begins with a brief introduction to the basic theory of PS materials in Section II. Subsequently, Section III and IV derive and solve the coupling equation system of variable cross-section bending PS fibers. Finally, the simulation results and discussions are presented in Section V and VI.

II. BASIC EQUATIONS OF PIEZOELECTRICITY

This section presents the description of the electromechanical coupling behaviors of PSs using a Cartesian tensor system of three-dimensional differential equations. The field equations, which include the motion equation, Gauss's theorem in electrostatics, and the continuity equation of holes and electron charges, are provided as follows[21–23]:

$$\begin{aligned} &T_{ji,j} = \rho \ddot{u}_i \\ &D_{i,i} = q(p - n + N_D^+ - N_A^-) \\ &J_{i,i}^p = -q\dot{p} \\ &J_{i,i}^n = q\dot{n} \end{aligned} \tag{1}$$

Here a partial derivative concerning the coordinate associated with the index is indicated by a comma after the index, while a time derivative is shown as a dot that is superimposed. T_{ji}, u_i, and D_i are the components of the stress tensor, mechanical displacement vector, and electric displacement vector, respectively. The elementary charge and mass density are denoted by q and ρ. p and n are the concentrations of holes and electrons, therefore J_i^p and J_i^n represent the hole and electron current densities. According to the theory of drift-diffusion of currents in semiconductors[21], they can be expressed as:

$$\begin{aligned} &J_i^p = qp\mu_{ij}^p E_j - qD_{ij}^p p_{,j} \\ &J_i^n = qn\mu_{ij}^n E_j + qD_{ij}^n n_{,j} \end{aligned} \tag{2}$$

E_j is the electric field component here. μ_{ij}^p and μ_{ij}^n are the hole and electron mobility, D_{ij}^p and D_{ij}^n are the hole and electron diffusion coefficients. The equations above demonstrate that the total current in the semiconductor consists of two terms: the drift term caused by the electric field driving the carrier motion and the diffusion term caused by the carrier concentration gradient.

In PSs, the force equilibrium equations are coupled to the electrical equations through the following constitutive relationship:

$$\begin{aligned} &T_{ij} = c_{ijkl} S_{kl} - e_{kij} E_k \\ &D_i = \varepsilon_{ij} E_j + e_{ijk} S_{jk} \end{aligned} \tag{3}$$

S_{ij} is the strain component, c_{ijkl}, e_{kij} and ε_{ij} are the elastic constant, piezoelectric constant, and dielectric constant of the material, respectively.

The relationship between strain and displacement, electric field and potential are:

$$\begin{aligned} &S_{ij} = \frac{1}{2}(u_{i,j} + u_{j.i}) \\ &E_i = -\varphi_{,i} \end{aligned} \tag{4}$$

To linearize the equation, the carrier concentration is usually represented in the analytical model as a perturbation in the form of:

$$\begin{aligned} &p = p_0 + \Delta p \\ &n = n_0 + \Delta n \\ &p_0 = N_A^- \\ &n_0 = N_D^+ \end{aligned} \tag{5}$$

In Equation (5), Δn and Δp are the perturbations of electron concentration and hole concentration respectively. In this case, Gauss theorem and the continuity equation in (1) become:

$$\begin{aligned} &D_{i,i} = q(\Delta p - \Delta n) \\ &q\frac{\partial}{\partial t}(\Delta p) = -J_{i,i}^p \\ &q\frac{\partial}{\partial t}(\Delta n) = J_{i,i}^n \end{aligned} \tag{6}$$

The current Equation (2) is linearized as:

$$\begin{aligned} &J_i^p = qp_0\mu_{ij}^p E_j - qD_{ij}^p (\Delta p)_{,j} \\ &J_i^n = qn_0\mu_{ij}^n E_j + qD_{ij}^n (\Delta n)_{,j} \end{aligned} \tag{7}$$

The linearized equations mentioned above have been successfully applied to study the static and dynamic problems of various structures such as PS rods[10,20,24,25], beams[26–28], plates[29–33], tubes[34,35], and blocks[11,36–38].

III. COUPLED EQUATIONS OF BENT PS FIBER

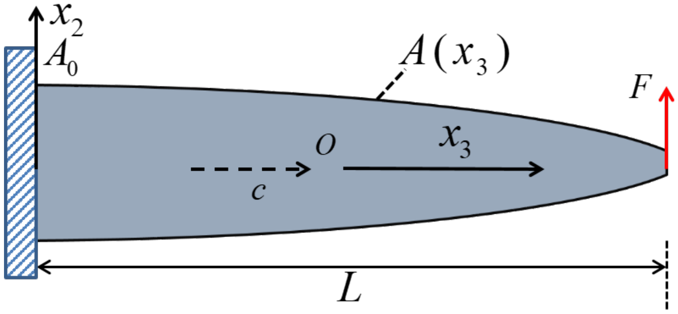

Figure 1: Sketch of the bent PS fiber with variable cross-section.

Consider the bending deformation of the PS fiber with variable cross-sections shown in Figure 1. The length of the fiber is L. The cross-sectional area A varies along the x_3 axis. Also, the fiber has its left end fixed and a shear force F is applied at its right end. The c axis is in the same direction as the x_3 axis, which locates along the central line with its origin set at the left end surface.

Referring to the Mindlin plate theorem, power series expansions of displacement, potential, and internal carrier concentration variations with first-order approximation are[39–41]:

$$\begin{aligned} u_2 &\cong v(x_3,t) \\ u_3 &\cong x_2\psi(x_3,t) \\ \varphi &\cong x_2\phi^1(x_3,t) \\ \Delta n &\cong x_2 n^1(x_3,t) \\ \Delta p &\cong x_2 p^1(x_3,t) \end{aligned} \tag{8}$$

Here v is the deflection and ψ is the deflection-related shear deformation. ϕ^1, n^1, and p^1 are the first-order coefficients describing the transverse distribution of the potential, variations of electron and hole concentrations, respectively. The corresponding strain, electric field, and carrier concentration gradient can be expressed as:

$$\begin{aligned} &S_3 = x_2\psi_{,3} && S_4 = v_{,3}+\psi \\ &E_2 = -\phi^1 && E_3 = -x_2\phi^1_{,3} \\ &\Delta n_{,2} = n^1 && \Delta n_{,3} = x_2 n^1_{,3} \\ &\Delta p_{,2} = p^1 && \Delta p_{,3} = x_2 p^1_{,3} \end{aligned} \tag{9}$$

Using the stress relaxation condition, the expressions for the stress and electric displacement can be derived from Equation (3) in Section I:

$$\begin{aligned} T_3 &= \bar{c}_{33}S_3 - \bar{e}_{33}E_3 = \bar{c}_{33}x_2\psi_{,3} + \bar{e}_{33}x_2\phi^1_{,3} \\ T_4 &= \bar{c}_{44}S_4 - \bar{e}_{15}E_2 = \bar{c}_{44}(v_{,3}+\psi) + \bar{e}_{15}\phi^1 \\ D_2 &= \bar{e}_{15}S_4 + \bar{\varepsilon}_{11}E_2 = \bar{e}_{15}(v_{,3}+\psi) - \bar{\varepsilon}_{11}\phi^1 \\ D_3 &= \bar{e}_{33}S_3 + \bar{\varepsilon}_{33}E_3 = \bar{e}_{33}x_2\psi_{,3} - \bar{\varepsilon}_{33}x_2\phi^1_{,3} \end{aligned} \tag{10}$$

The material constants in Equation (10) satisfy the following relationship:

$$\begin{aligned} &\bar{c}_{33} = 1/s^E_{33} && \bar{c}_{44} = 1/s^E_{44} \\ &\bar{e}_{33} = d_{33}/s^E_{33} && \bar{e}_{15} = d_{15}/s^E_{44} \\ &\bar{\varepsilon}_{11} = \varepsilon^T_{11} - (d_{15})^2/s^E_{44} && \bar{\varepsilon}_{33} = \varepsilon^T_{33} - (d_{33})^2/s^E_{33} \end{aligned} \tag{11}$$

Here $\bar{c}_{33}$, $\bar{e}_{33}$ and $\bar{\varepsilon}_{33}$ are the one-dimensional equivalent elastic constants, piezoelectric constants and dielectric constants. The constitutive relationships of the current are:

$$\begin{aligned} J^n_2 &= qn_0\mu^n_{22}E_2 + qD^n_{22}\Delta n_{,2} = -qn_0\mu^n_{22}\phi^1 + qD^n_{22}n^1 \\ J^n_3 &= qn_0\mu^n_{33}E_3 + qD^n_{33}\Delta n_{,3} = -qn_0\mu^n_{33}x_2\phi^1_{,3} + qD^n_{33}x_2 n^1_{,3} \\ J^p_2 &= qp_0\mu^n_{22}E_2 - qD^p_{22}\Delta p_{,2} = -qp_0\mu^n_{22}\phi^1 - qD^n_{22}p^1 \\ J^p_3 &= qp_0\mu^n_{33}E_3 - qD^p_{33}\Delta p_{,3} = -qp_0\mu^n_{33}x_2\phi^1_{,3} - qD^n_{33}x_2 p^1_{,3} \end{aligned} \tag{12}$$

The bending moment M, shear force Q and the equivalent electric displacement D^0_2 and D^1_3 in the structure can be derived from the following constitutive relationships:

$$\begin{aligned} M &= \textstyle\int_A x_2T_3dA = \bar{c}_{33}I\psi_{,3} + \bar{e}_{33}I\phi^1_{,3} \\ Q &= \textstyle\int_A T_4dA = \bar{c}_{44}A(v_{,3}+\psi) + \bar{e}_{15}A\phi^1 \\ D^0_2 &= \textstyle\int_A D^{(1)}_2dA = \bar{e}_{15}A(v_{,3}+\psi) - \bar{\varepsilon}_{11}A\phi^1 \\ D^1_3 &= \textstyle\int_A x_2D^{(1)}_3dA = \bar{e}_{33}I\psi_{,3} - \bar{\varepsilon}_{33}I\phi^1_{,3} \end{aligned} \tag{13}$$

where the cross-sectional rotational inertia I can be expressed as:

$$I = \frac{A^2}{4\pi} \tag{14}$$

The current relationship can also be obtained by integrating over the cross-section:

$$\begin{aligned} J^{n0}_2 &= \textstyle\int_A J^n_2dA = -qn_0\mu^n_{22}A\phi^1 + qD^n_{22}An^1 \\ J^{n1}_3 &= \textstyle\int_A x_2J^n_3dA = qn_0\mu^n_{33}I\phi^1_{,3} + qD^n_{33}In^1_{,3} \\ J^{p0}_2 &= \textstyle\int_A J^p_2dA = -qp_0\mu^n_{22}A\phi^1 - qD^n_{22}Ap^1 \\ J^{p1}_3 &= \textstyle\int_A x_2J^p_3dA = qp_0\mu^n_{33}I\phi^1_{,3} - qD^n_{33}Ip^1_{,3} \end{aligned} \tag{15}$$

Assuming that the model in Figure 1 is n-type PS fiber, the total field equation in static equilibrium can be written as:

$$\begin{aligned} &Q_{,3} = 0 \\ &M_{,3} - Q = 0 \\ &D^1_{3,3} - D^0_2 = -qIn^1 \\ &J^{n1}_{3,3} - J^{n0}_2 = 0 \end{aligned} \tag{16}$$

The boundary conditions are:

$$\begin{aligned} &v(0) = 0 && M(L) = 0 && \psi(0) = 0 && Q(L) = F \\ &D^{(1)}_3(0) = 0 && D^{(1)}_3(L) = 0 && J^{n(1)}_3(0) = 0 && J^{n(1)}_3(L) = 0 \end{aligned} \tag{17}$$

IV. FIELD DISTRIBUTION ANALYSIS

Substituting equations (13) and (15) into Equation (16), the exact expressions of the field equation are obtained:

$$\begin{aligned}
&\bar{c}_{33}I\psi_{,33}+\bar{c}_{33}I_{,3}\psi_{,3}+\bar{e}_{33}I\phi^{(1)}_{,33}+\bar{e}_{33}I_{,3}\phi^{(1)}_{,3}-\bar{c}_{44}A(v_{,3}+\psi)-\bar{e}_{24}A\phi^{(1)}=0\\
&\bar{c}_{44}A(v_{,33}+\psi_{,3})+\bar{c}_{44}A_{,3}(v_{,3}+\psi)+\bar{e}_{24}A\phi^{(1)}_{,3}+\bar{e}_{24}A_{,3}\phi^{(1)}=0\\
&\bar{e}_{33}I\psi_{,33}+\bar{e}_{33}I_{,3}\psi_{,3}-\bar{\varepsilon}_{33}I\phi^{(1)}_{,33}-\bar{\varepsilon}_{33}I_{,3}\phi^{(1)}_{,3}-\bar{e}_{24}A(v_{,3}+\psi)+\bar{\varepsilon}_{22}A\phi^{(1)}=-qIn^{(1)}\\
&-qn_0\mu^n_{33}I\phi^{(1)}_{,33}-qn_0\mu^n_{33}I_{,3}\phi^{(1)}_{,3}+qD^n_{33}In^{(1)}_{,33}+qD^n_{33}I_{,3}n^{(1)}_{,3}+qn_0\mu^n_{11}A\phi^{(1)}-qD^n_{11}An^{(1)}=0
\end{aligned} \tag{18}$$

In this article, the system of partial differential equations in Equation (18) is difficult to solve analytically due to the variable parameters along x_3 axis, i.e., the cross-sectional area A and the rotational inertia I. Therefore, a numerical calculation method called the generalized differential quadrature method (GDQM) will be used to discretely solve the equations. The GDQM was proposed by Shu[42] and is an extension of the differential quadrature method (DQM)[43]. The DQM can obtain highly accurate numerical results with considerably fewer grid points than conventional low-order finite difference and finite element methods, requiring relatively little computational effort. The GDQM was developed in the late 1980s to solve the ill-conditioned algebraic equations generated by early DQM and to release the restriction on the number of grid points. As a result, the GDQM has emerged as a powerful numerical discretization tool in recent years and has been efficiently employed in a wide range of problems in engineering and physical sciences.

In the GDQM approach, the value of the derivative at each node is represented as a weighted sum of the function values at the discrete points, which define the domain of the function. According to GDQM, the s-order partial differential of the continuous differentiable function $f(x)$ can be expressed as (for the sake of clarity, the x_3 axis is written directly as x in the following equations, while x_i denotes the coordinates of the ith discrete point):

$$\frac{\partial^s f(x)}{\partial x^s}\Big|_{x=x_i}=\sum_{j=1}^{R}B^{[s]}_{ij}f(x_j)\qquad i=1,2...R \tag{19}$$

where R is the number of discrete points and $B^{[s]}_{ij}$ is the s-order weighted coefficient matrix. For the problems in this section, the variables v, ψ, ϕ_1 and n_1 are expressed in the following form:

$$\{v,\psi,\phi^1,n^1\}=\sum_{j=1}^{R}L_j(x)\{\mathrm{V}_j,\Psi_j,\Phi_j,\mathrm{N}_j\} \tag{20}$$

where $L_j(x)$ is the Lagrangian polynomial:

$$L_j(x)=\prod_{\substack{k=1\\k\neq j}}^{R}\frac{x-x_k}{x_j-x_k} \tag{21}$$

According to Equation (19), the s-order derivatives of Equation (20) are:

$$\left\{v^{[s]}(x_i),\psi^{[s]}(x_i),\phi^{1[s]}(x_i),n^{1[s]}(x_i)\right\}=\sum_{j=1}^{R}B^{[s]}_{ij}\{\mathrm{V}_j,\Psi_j,\Phi_j,\mathrm{N}_j\} \tag{22}$$

Here the expression of the first-order weighted coefficient matrix $B^{[1]}_{ij}$ is:

$$B^{[1]}_{ij}=L^{[1]}_j(x_i)=\begin{cases}\prod\limits_{\substack{k=1\\k\neq i,j}}^{R}(x_i-x_k)\Big/\prod\limits_{\substack{k=1\\k\neq j}}^{R}(x_j-x_k) & (i\neq j)\\ \sum\limits_{\substack{k=1\\k\neq i}}^{R}\frac{1}{(x_i-x_k)} & (i=j)\end{cases} \tag{23}$$

The remaining higher-order weighting coefficients matrix can be obtained by multiplying the lower-order weighting coefficient matrix:

$$B^{[s+1]}_{ij}=B^{[1]}_{ij}B^{[s]}_{ij} \tag{24}$$

For selecting discrete points, we adopt the Chebyshev-Gauss-Lobatto point system[42] with the following distribution:

$$x_i=\frac{1}{2}\left[1-\cos\left(\frac{i-1}{R-1}\pi\right)\right] \tag{25}$$

Employing Equation (22), the field Equation (18) at each discrete point $(1<i<R)$ in the domain becomes:

$$\begin{aligned}
&\bar{c}_{33}I(x_i)\sum_{j=1}^{R}B^{[2]}_{ij}\Psi_j+\bar{c}_{33}I_{,3}(x_i)\sum_{j=1}^{R}B^{[1]}_{ij}\Psi_j+\bar{e}_{33}I(x_i)\sum_{j=1}^{R}B^{[2]}_{ij}\Phi_j+\bar{e}_{33}I_{,3}(x_i)\sum_{j=1}^{R}B^{[1]}_{ij}\Phi_j-\bar{c}_{44}A(x_i)(\sum_{j=1}^{R}B^{[1]}_{ij}\mathrm{V}_j+\Psi_i)-\bar{e}_{24}A(x_i)\Phi_i=0\\
&\bar{c}_{44}A(x_i)(\sum_{j=1}^{R}B^{[2]}_{ij}\mathrm{V}_j+\sum_{j=1}^{R}B^{[1]}_{ij}\Psi_j)+\bar{c}_{44}A_{,3}(x_i)(\sum_{j=1}^{R}B^{[1]}_{ij}\mathrm{V}_j+\Psi_i)+\bar{e}_{24}A(x_i)\sum_{j=1}^{R}B^{[1]}_{ij}\Phi_j+\bar{e}_{24}A_{,3}(x_i)\Phi_i=0\\
&\bar{e}_{33}I(x_i)\sum_{j=1}^{R}B^{[2]}_{ij}\Psi_j+\bar{e}_{33}I_{,3}(x_i)\sum_{j=1}^{R}B^{[1]}_{ij}\Psi_j-\bar{\varepsilon}_{33}I(x_i)\sum_{j=1}^{R}B^{[2]}_{ij}\Phi_j-\bar{\varepsilon}_{33}I_{,3}(x_i)\sum_{j=1}^{R}B^{[1]}_{ij}\Phi_j-\bar{e}_{24}A(x_i)(\sum_{j=1}^{R}B^{[1]}_{ij}\mathrm{V}_j+\Psi_i)+\bar{\varepsilon}_{22}A(x_i)\Phi_i+qI(x_i)\mathrm{N}_i=0\\
&-n_0\mu^n_{33}I(x_i)\sum_{j=1}^{R}B^{[2]}_{ij}\Phi_j-n_0\mu^n_{33}I_{,3}(x_i)\sum_{j=1}^{R}B^{[1]}_{ij}\Phi_j+D^n_{33}I(x_i)\sum_{j=1}^{R}B^{[2]}_{ij}\mathrm{N}_j+D^n_{33}I_{,3}(x_i)\sum_{j=1}^{R}B^{[1]}_{ij}\mathrm{N}_j+n_0\mu^n_{11}A(x_i)\Phi_i-D^n_{11}A(x_i)\mathrm{N}_i=0
\end{aligned} \tag{26}$$

Meanwhile, according to the boundary conditions in Equation (17), the following conditions are satisfied at the two discrete points on the boundary:

$$\begin{aligned}
&\mathrm{V}_1 = 0 \\
&\bar{c}_{33} I(x_R) \sum_{j=1}^{R} B_{Rj}^{[1]} \Psi_j + \bar{e}_{33} I(x_R) \sum_{j=1}^{R} B_{Rj}^{[1]} \Phi_j = 0 \\
&\Psi_1 = 0 \\
&\bar{c}_{44} A(x_R) \Big(\sum_{j=1}^{R} B_{Rj}^{[1]} \mathrm{V}_j + \Psi_R \Big) + \bar{e}_{24} A(x_R) \Phi_R = F \\
&\bar{e}_{33} I(x_1) \sum_{j=1}^{R} B_{1j}^{[1]} \Psi_j - \bar{\varepsilon}_{33} I(x_1) \sum_{j=1}^{R} B_{1j}^{[1]} \Phi_j = 0 \\
&\bar{e}_{33} I(x_R) \sum_{j=1}^{R} B_{Rj}^{[1]} \Psi_j - \bar{\varepsilon}_{33} I(x_R) \sum_{j=1}^{R} B_{Rj}^{[1]} \Phi_j = 0 \\
&-n_0 \mu_{33}^{n} I(x_1) \sum_{j=1}^{R} B_{1j}^{[1]} \Phi_j + D_{33}^{n} I(x_1) \sum_{j=1}^{R} B_{1j}^{[1]} \mathrm{N}_j = 0 \\
&-n_0 \mu_{33}^{n} I(x_R) \sum_{j=1}^{R} B_{Rj}^{[1]} \Phi_j + D_{33}^{n} I(x_R) \sum_{j=1}^{R} B_{Rj}^{[1]} \mathrm{N}_j = 0
\end{aligned} \tag{27}$$

The field distributions at each discrete point can be obtained by solving the system of linear equations consisting of equations (26) and (27) using MATLAB.

V. NUMERICAL RESULTS AND DISCUSSION

In this section, the materials of the PS fiber are chosen as ZnO, whose material constants are listed in Table I. Besides, the parameters of the PS fibers we used are shown in Table II.

A. First-order variation of cross-sectional area

In this subsection, we consider fibers with first-order variation in cross-sectional area. The area variation profile of the fibers is chosen to be:

$$A = A_0 - \lambda \times A_0 x / L \tag{28}$$

Here in Equation (28), λ represents the taper of the fiber. The sharpness of the PS fiber increases with increasing λ. Therefore, the radius distribution of the fibers, i.e. the shape of the profile, is shown in Figure 2. Firstly, the convergence and correctness of the algorithm we used need to be verified. When $A_0 = 2.598 \times 10^{-14}\ m^2$, $F = 0.02\ nN$, and $\lambda = 0.6$, the n^1 distributions obtained by choosing different numbers of discrete points R are shown in Figure 3. The number of discrete points, denoted by R, is found to affect the smoothness of the distribution curve, with the curve shape remaining relatively unchanged when R is greater than 50. For the numerical calculations in this paper, R is set to 200. FEM results given by COMSOL Multiphysics are used to validate the GDQM results. Figure 3 also compares the n^1 distribution computed by the GDQM with those computed by FEM. The results indicate that the computed n^1 distributions from FEM and GDQM are in agreement, thus validating the theoretical analysis using the GDQM method.

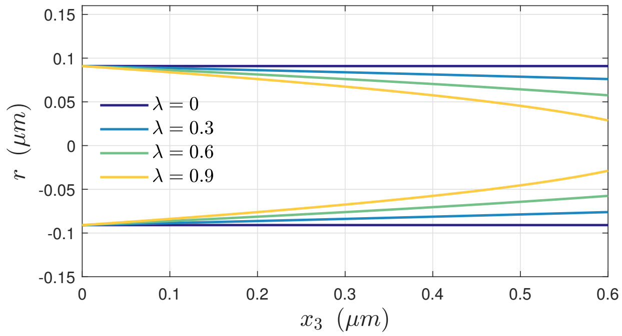

Figure 2: Fiber radius distribution with first-order variation in cross-sectional area for different values of λ

Table I: Material constants of ZnO

Notation	Description	Value
s_{33}^{E}	Elastic compliance constant	$6.94 \times 10^{-12}\ m^2/N$
d_{33}	Piezoelectric constant	$11.67 \times 10^{-12}\ C/N$
ε_{33}^{T}	Dielectric constant	$1.12 \times 10^{-10}\ F/m$
q	Elementary charge	$1.602 \times 10^{-19}\ C$
$k_B T/q$	Thermal voltage at 300 K	$0.0259\ V$

Table II: Parameter settings in Section V

Notation	Description	Value
L	Length of the fiber	$0.6\ \mu m$
A_l	Area of the left end surface	$2.598 \times 10^{-14}\ m^2$
A_r	Area of the right end surface	Varies with function $A(x)$
F	Applied end force	$2\ nm$
n_0	Initial electron concentration	$10^{21}\ m^{-3}$

Next, the impact of variable cross-section on the distribution of electromechanical fields within the fiber is explored. With an external force of $F = 0.02\ nN$, Figure 4 displays the electromechanical field distributions for various values of λ.

The distribution of deflection v and shear deformation ψ are presented in Figure 4(a) and 4(b), respectively. The results indicate that an increase in the parameter λ leads to larger values of both deflection v and shear deformation ψ. This can be attributed to the contraction of the right part of the fiber with increasing λ, which makes deformation easier. In addition, Figure 4(c) and 4(d) depict the distribution of one-dimensional potential ϕ^1 and electron concentration variation n^1. When $\lambda = 0$, the fiber is uniform along the x_3 axis, and the results indicate that only ϕ^1 and n^1 near the left end of the fiber exhibit drastic variations, while those in the remaining part of the fiber remain nearly constant. This finding is in agreement with previous studies[44,45], which suggested that the distribution of electrical quantities in bending-deformed uniform PS fibers is independent of the axial direction. In con-

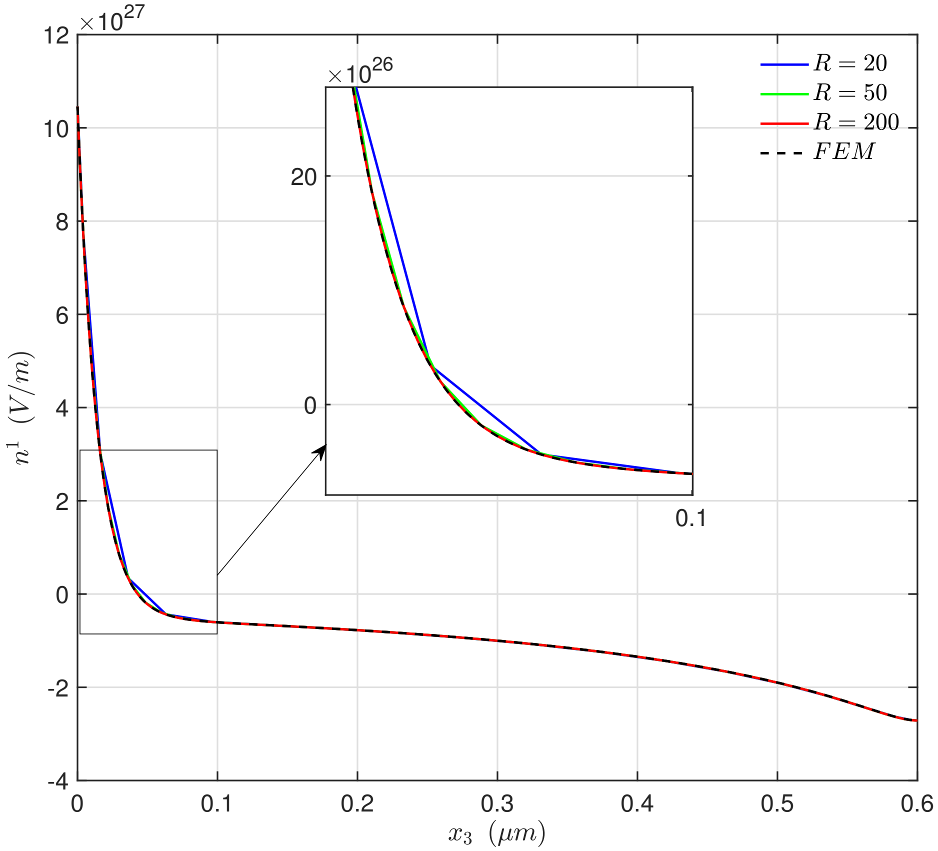

Figure 3: The distribution of the electron concentration variation n^1 for correctness and convergence verification

trast to the previous findings in uniform fibers, in non-uniform fibers, the distribution of electrical quantities changes along the axial direction as the strain parameter λ increases. The change in potential ϕ^1 and electron concentration n^1 is more significant near the right end of the fiber due to the specific strain distribution. In addition, the distribution of the shear strain S_4 is shown in Figure 4(e). It can be seen that S_4 is basically constant along the axial direction for $\lambda = 0$. However, as λ increases, S_4 becomes larger on the right side of the fiber, leading to a more significant variation in potential and carrier concentration.

In the following study, the value of λ is fixed while varying the external force F to examine the field distribution. The distribution of one-dimensional potential ϕ^1 in Figure 5(a) changes dramatically as expected, with changes occurring simultaneously with opposite signs near both ends, which is in contrast to Figure 4(c), where the field changes only at one end. This is because, as shown in Figure 5(b), the variation of F affects the distribution of shear strain S_4 along the whole fiber, whereas, in Figure 4(e), S_4 is essentially unchanged at the left end due to the fixed surface area.

In the context of their use as energy harvesters and sensors, the potential distribution on the fiber surface is of more practical concern. However, as can be seen from Equation (8), the ϕ^1 discussed in Figure 4 and 5 represents only the one-dimensional coefficients of the two-dimensional potential distribution, while the potential distribution on the fiber surface equals to $\phi^1 \times r$, where r is the fiber radius. Thus, although the value of ϕ^1 in Figure 4(c) varies monotonically along the x_3 axis with increasing λ, it does not necessarily indicate that the potential distribution on the surface of the fiber also varies monotonically. This is because the surface potential is determined by the product of the potential and the fiber section radius. In the case of $\lambda > 0$, the potential rises rapidly, but the section radius r also shrinks abruptly near the right end of the section. The higher-order terms in the product can cause local poles in the potential along the axial direction. Figure 6 shows the potential distribution φ on the lower surface of the fiber corresponding to the values of λ considered in Figure 4. It can be observed that, for the fiber with $\lambda = 0.9$, the surface potential has an extreme point near the right end. To further illustrate this phenomenon, analyze the causes of the phenomenon and thus control this property, different forms of cross-sectional area functions are chosen and the corresponding surface potentials are calculated and compared in the next subsection.

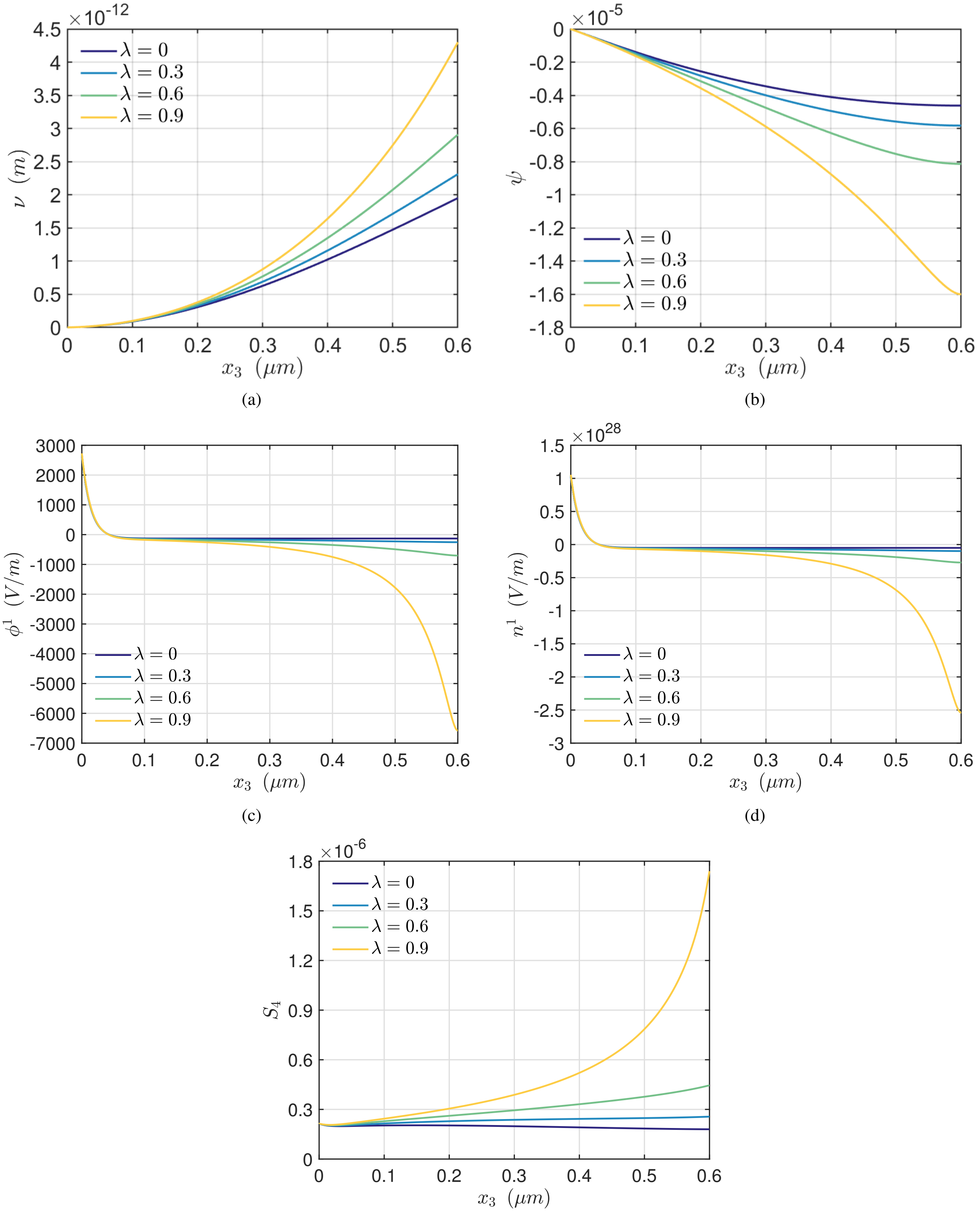

Figure 4: The distribution of the electromechanical fields for different values of λ: (a) deflection ν; (b) shear deformation ψ; (c) electric potential ϕ^1; (d) electron concentration variation n^1; (e) shear strain S_4

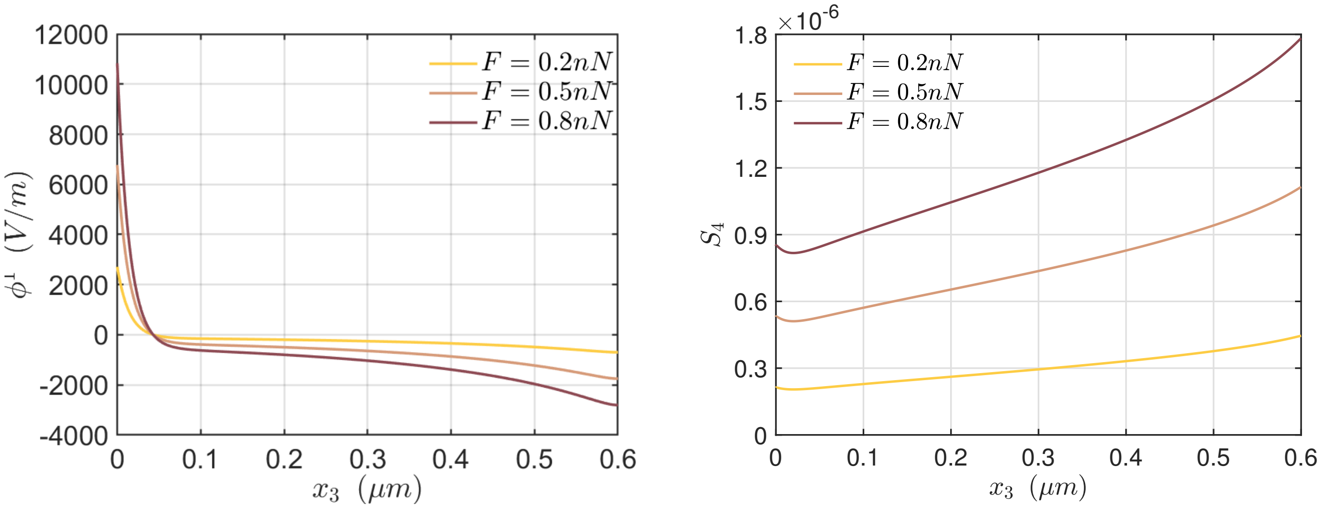

(a)

(b)

Figure 5: Distributions of the electromechanical field under different magnitudes of external forces F: (a) potential ϕ^1; (b) shear strain S_4

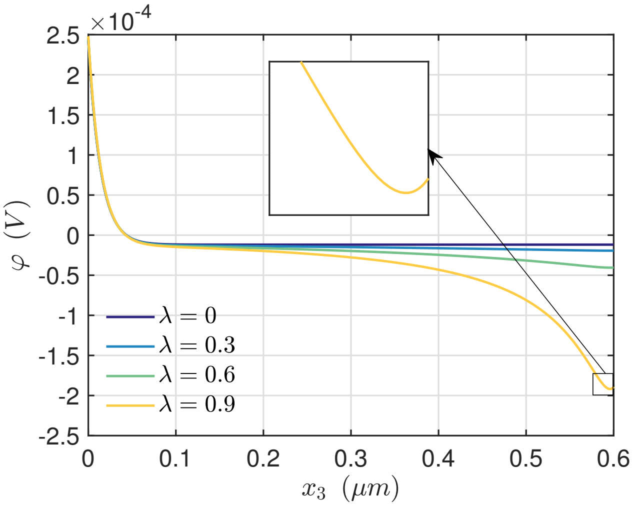

Figure 6: Distribution of surface potential φ for different values of λ

B. Analysis of surface potential extreme point phenomenon

In response to the phenomenon discovered in the previous section, where a bending fiber with a monotonic change in cross-sectional area exhibits a surface potential extremum, this study first used COMSOL software to perform three-dimensional modeling and simulation calculations to verify the existence of this phenomenon. The results showed that, under the action of bending deformation, the variable cross-sectional fiber did exhibit a potential extremum near the right end face when λ approaches 1, confirming the existence of this phenomenon and the necessity of this study. The simulation process is presented in the appendix.

In this section, the comparison was made among five different cross-sectional area functions of the bent and deformed cross-sectional area fibers. These five fibers' cross-sectional area functions are listed in Table III. The left-end cross-sectional area of these fibers is fixed at a uniform value A_0, and the cross-sectional area decreases monotonically with increasing x, with the smallest cross-sectional area at the right end. Among the five functions, μ uniformly represents the contraction amplitude of the fiber's right-end surface compared to the left-end surface, i.e., the ratio of the right-end cross-sectional area to the left-end cross-sectional area. Specifically, when $\mu = 0$, the fiber is uniform, and the cross-sectional area does not change. When $\mu = 1$, the right-end cross-sectional area is 0, that is, the right end of the fiber becomes a sharp point. The parameter μ is selected at values of $3/4$, $15/16$, $63/64$, and $255/256$, which correspond to the right end face radius contracting to half, one-fourth, one-eighth, and one-sixteenth of the maximum radius. The five cross-sectional area functions are sorted according to the concavity and convexity of their corresponding radius functions, from the concave function to the linear function to the convex function. The radius function corresponding to the cross-sectional area function of number 3 is linear.

Table III: Area formulas for comparison

No.	Formula	When $x = L$ and $\mu \to 1$
1	$A = A_0 - \mu \times A_0 x^2/L^2$	$r \to 0$; $dr/dx < 0$
2	$A = A_0 - \mu \times A_0 x/L$	$r \to 0$; $dr/dx < 0$
3	$A = A_0(1-(1-\sqrt{1-\mu}) \times x/L)^2$	$r \to 0$; $dr/dx < 0$
4	$A = (1-\mu) \times A_0 + \mu \times A_0(L-x)^2/L^2$	$r \to 0$; $dr/dx \to 0$
5	$A = (1-\mu) \times A_0 + \mu \times A_0(L-x)^3/L^3$	$r \to 0$; $dr/dx \to 0$

The area distribution of the radius r and the corresponding surface potential φ results are displayed in Figure 7. As

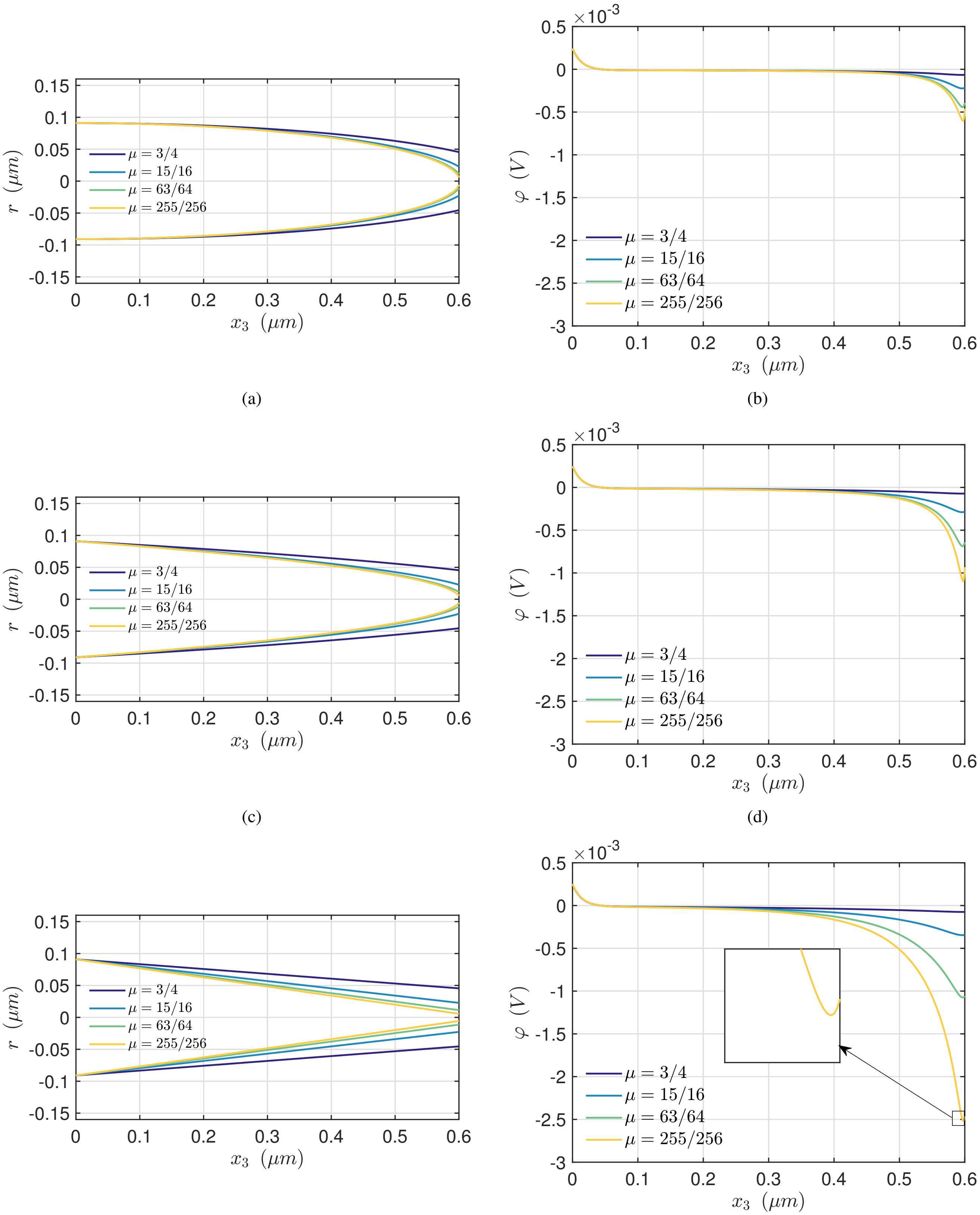
$\times 10^{-3}$
$r\ (\mu m)$
$\varphi\ (V)$
$x_3\ (\mu m)$
$\mu = 3/4$
$\mu = 15/16$
$\mu = 63/64$
$\mu = 255/256$
0.15
0.1
0.05
0
-0.05
-0.1
-0.15
0.5
-0.5
-1
-1.5
-2
-2.5
-3
0
0.1
0.2
0.3
0.4
0.5
0.6

(a)

(b)

(c)

(d)

(e)

(f)

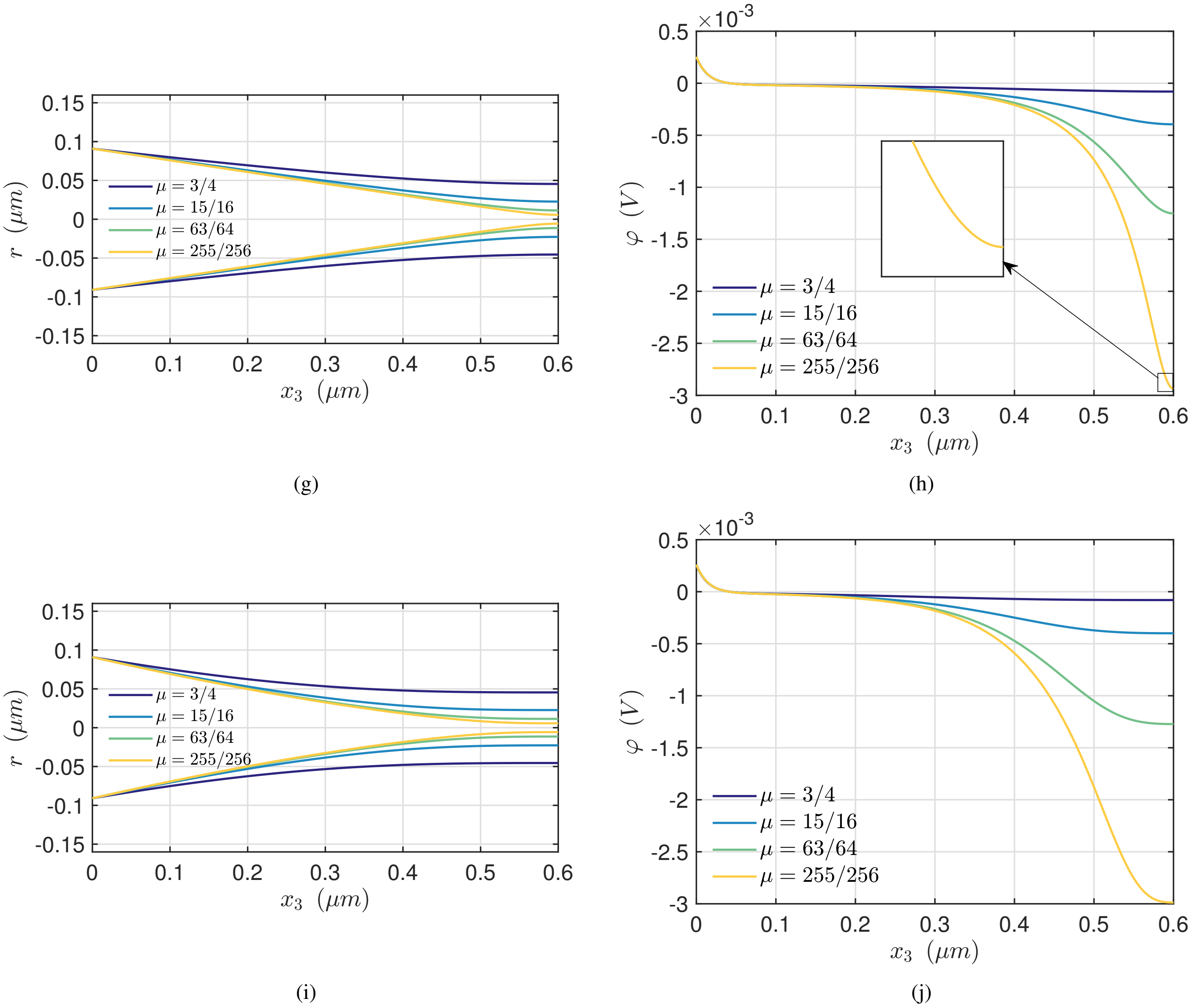

Figure 7: The corresponding radius r distribution and surface potential distribution φ of fibers with different cross-sectional area functions A

shown in Figure 7, as the convexity of the functions increases, the overall contraction of the fibers also increases, and the amplitude of the surface potential increases accordingly. Although the cross-sectional areas of these fibers are all monotonically decreasing functions, in Figure 7(b),7(d) and 7(f), a surface potential extremum appears as the contraction rate μ increases, while no extremum appears in Figure 7(h) and 7(j) and the slope of the surface potential φ approaches 0 at the right end.

This phenomenon is consistent with the results obtained from the theoretical formulas in the previous section. For fibers with a monotonically decreasing cross-sectional area under bending, although the monotonically changing cross-sectional area leads to the monotonically changing electric potential phi1 per unit length, the two-dimensional surface electric potential $\varphi = \phi^1 \times r$. Even though the absolute value of phi1 increases continuously, r is decreasing and approaching 0. When the slope of r reaches a certain value, it will inevitably lead to the extreme point of the surface potential φ. Therefore, we can conclude that the appearance of extreme points is related to the concavity and convexity of the cross-sectional radius r, or in other words, to the way that r approaches 0. Moreover, when r is a linear or higher-order concave function, extremum points will appear when approaching 0 on the right-end surface. When r is a convex function and the slope of r approaches 0 on the right end surface, the surface potential will not have extremum points.

The appearance of an extreme point at the right end can also be understood from a physical perspective. When considering the limiting case where the cross-sectional area at the right end equals zero, the surface potential $\varphi = 0$. This inevitably leads to the fact that the absolute value of the surface potential φ cannot increase without limit. Therefore, when the cross-sectional area at the right end is close to or relatively small, an extreme point will naturally appear near the right end, and the surface potential φ will rapidly decrease. However, when the slope of the radius r also tends to 0 at the right end, the extreme point no longer appears, which can be understood from another physical perspective. When the slope of r approaches zero, it can be understood that for that small section, the fiber is uniform. Based on previous studies on uniform fibers, we know that the surface potential on uniform fibers remains constant. Therefore, near the right end where the cross-sectional area of the variable cross-section fiber does not change, the slope of the surface potential is zero, and thus no extreme point will appear.

In summary, to prevent the occurrence of surface potential extremum points, the following measures can be taken:

(1) Reduce the shrinkage rate μ of the fiber cross-sectional area and increase the minimum value of the fiber cross-sectional area.

(2) Properly set the radius distribution of the fiber, control the concavity and convexity of the r function, and reduce the absolute value of the slope of r at the contraction end face.

These measures can be achieved by adjusting the structural parameters of the fiber, thereby avoiding the occurrence of surface potential extremum points under bending, and ensuring the normal operation of the fiber. This has important practical significance for the design and optimization of equipment such as PS devices that work in bending mode.

C. Second-order variation of cross-sectional area

In this subsection, we examine PS fibers with variable cross-sectional areas of the second order. The expression for the cross-sectional area is given by Equation (29),

$$A = A_0 - \kappa \times A_0(xL - x^2)/L^2 \tag{29}$$

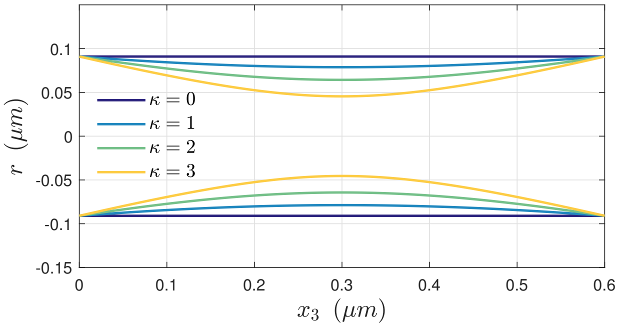

Figure 8: Fiber radius distribution with second-order variation in cross-sectional area for different values of κ

Equation (29) describes an hourglass-shaped fiber, where A_0 denotes the initial cross-sectional area, and κ represents the degree of shrinkage of the middle section relative to the two ends. When $\kappa = 0$, the cross-sectional area of the fiber remains constant, while when $\kappa = 3$, the middle cross-sectional area is one-fourth of the cross-sectional area at both ends. Figure 8 displays the radius distribution of the fibers.

To investigate the distribution of the electromechanical field in the fibers under different values of κ, we apply an external force of $F = 0.02\ \ nN$. The results are shown in Figure 9. Figure 9(a) and 9(b) show the deflection v and shear deformation ψ, respectively. As κ increases the values of v and ψ increase proportionally. This is because the smaller the cross-sectional area, the greater the deformation of the fiber under the same degree of external force. In particular, since the middle section of the fiber is the smallest, the slope of the middle part of the ψ distribution curve in Figure 9(b) is considerably higher than that of the two ends. The distribution of one-dimensional potential ϕ^1 and electron concentration variation n^1 are shown in Figure 4(c) and 4(d), respectively. In the case where $\kappa = 0$, the fibers are uniform, resulting in distribution patterns similar to those observed in the previous subsection for $\lambda = 0$. Specifically, the distribution of one-dimensional potential ϕ^1 and electron concentration variation n^1 undergo sharp changes only near the left end of the fiber, while the rest of the distribution remains essentially unchanged. However, in the nonuniform fibers in this subsection, as κ increases, ϕ^1 and n^1 not only vary along the axial direction but also exhibit sharp variations, leading to an extreme point in the middle of the fiber. The observed variation in ϕ^1 and n^1 is attributed to the generation of larger strain S_4 caused by the smaller cross-sectional area in the middle of the fiber. The distribution of the shear strain S_4 is shown in Figure 9(e), where an extreme point can be observed in the middle of the fiber. It is anticipated to have a corresponding effect on ϕ^1 and n^1.

Subsequently, to explore the response of fibers to different external forces F, κ was set to a constant value of 3. In Figure 10(a), the one-dimensional potential ϕ^1 exhibits significant variation, which is linear with the magnitude of the external force F. Moreover, the extremum always appears in the middle of the fiber, which is closely related to the shear strain S_4 shown in Figure 10(b). The trend of shear strain S_4 is always small at both ends and large in the middle. It is noteworthy that the extremum of the shear strain is always slightly to the left of the middle. This is because the shear strain is calculated as $S_4 = v_{,3} + \psi$, and the first term in the expression shifts the extreme point to the left. In addition, the surface potential distribution of the fibers was also studied, and the results are shown in Figure 11. As expected, at the point where the cross-sectional area has an extremum, there is also a corresponding extremum in the surface potential φ, with no shift. This means that if we need to artificially create extremums in the surface potential on the fiber, it can be achieved by changing the fiber contour and reasonably setting the cross-sectional area function of the fiber. This has significant implications for the design of nanoscale piezoelectric semiconductor devices.

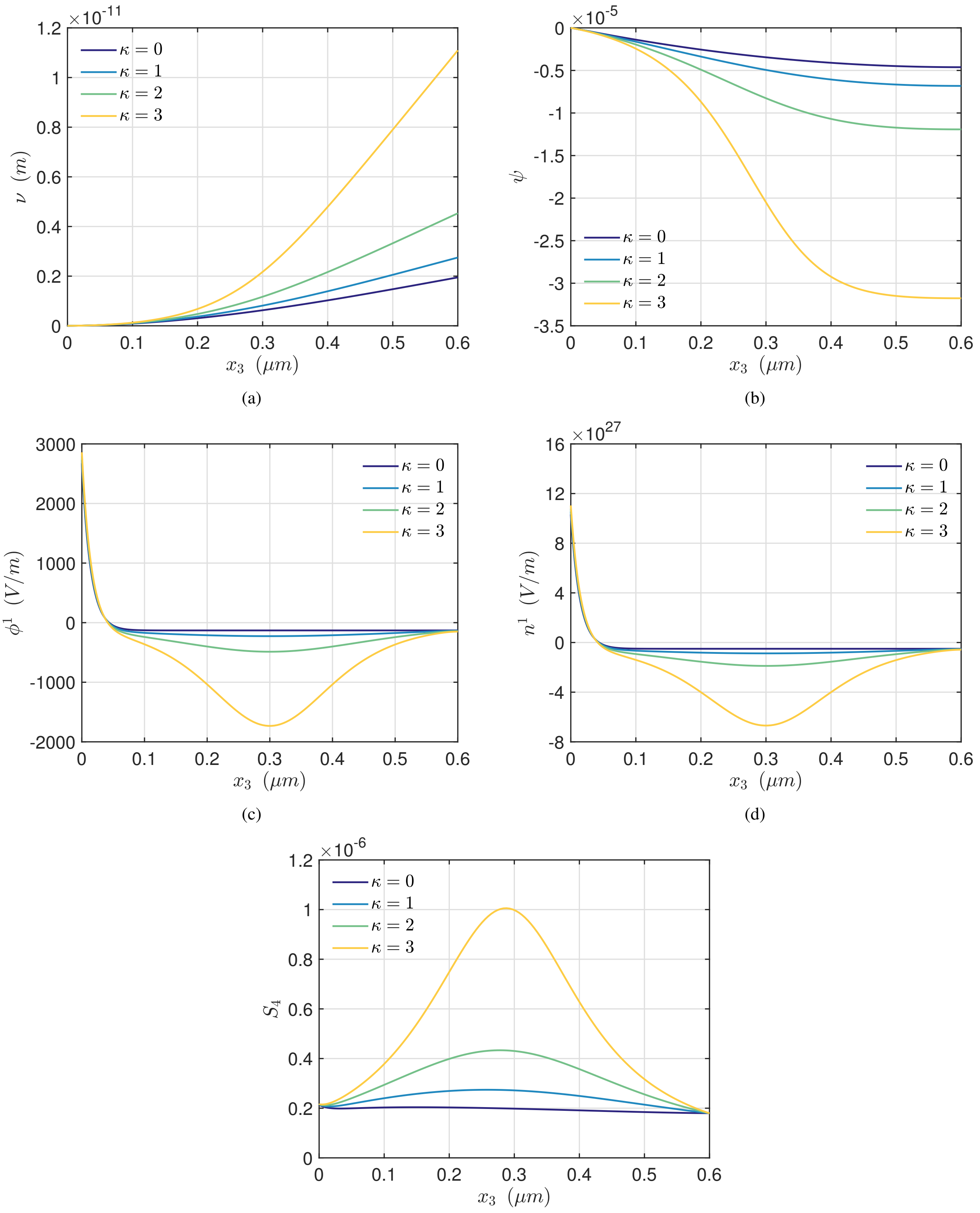

(a)

(b)

(c)

(d)

(e)

Figure 9: The distribution of the electromechanical fields for different values of κ: (a) deflection ν; (b) shear deformation ψ; (c) electric potential ϕ^1; (d) electron concentration variation n^1; (e) shear strain S_4

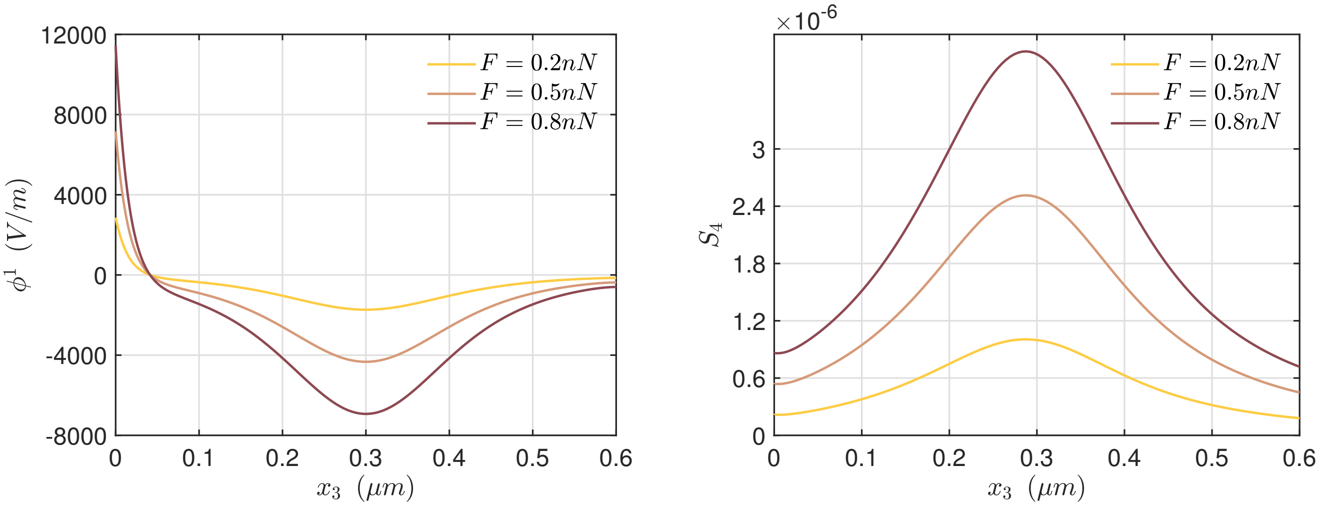

(a)

(b)

Figure 10: Distributions of the electromechanical field under different magnitudes of external forces F: (a) potential ϕ^1; (b) shear strain S_4

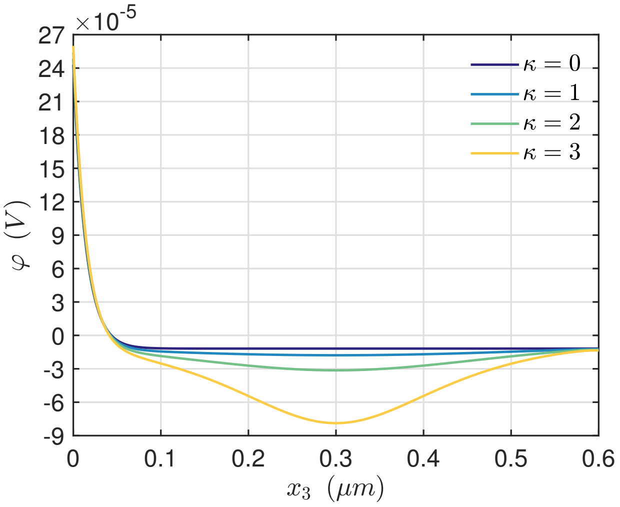

Figure 11: Distribution of surface potential φ for different values of κ

VI. CONCLUSIONS

In this paper, the electromechanical properties of PS fibers with variable cross-sections under bending deformation are investigated. The constitutive equations of two-dimensional variable cross-section fibers are derived using piezoelectric theory. The variable coefficient partial differential equation system describing the mechanical and electrical field distribution is solved using the numerical method GDQM. The main research findings of this study can be summarized as follows:

(1) Under the action of bending deformation, the distribution of electrical quantities of uniform PS fibers along the axial direction is uniform, while non-uniform fibers with variable cross-sections exhibit axial changes. At the same time, the electrical response of non-uniform fibers is more sensitive and intense compared to uniform fibers under the same external force.

(2) Under the action of bending deformation, contrary to superficial expectations, a monotonic change in the cross-sectional area does not necessarily lead to a corresponding monotonic change in the surface potential of PS fibers. The surface potential can sometimes exhibit extreme values, which depend on the convexity and concavity of the contour function of PS fibers.

(3) Under the action of bending deformation, it is possible to artificially create extremum points of the surface potential of PS fibers by setting extremum points on the fiber contour. When the contour function is quadratic, the extremum points of the contour coincide with those of the surface potential, while the shear strain will produce some deviation relative to the contour extremum points.

The research results of this paper can provide reliable theoretical guidance for the design of high-performance piezoelectric semiconductor nano-devices, and provide new ideas for manufacturing more efficient nano-generators and mechanical strain sensors in the future.

ACKNOWLEDGMENTS

This work was supported by the National Natural Science Foundation of China (12061131013, 11972276, 12172171, and 12211530064), the State Key Laboratory of Mechanics and Control of Mechanical Structures at NUAA (No. MCMS-I-0522G01), the Fundamental Research Funds for the Central Universities (NS2022011 and NE2020002), National Natural Science Foundation of Jiangsu Province (BK20211176), Local Science and Technology Development Fund Projects Guided by the Central Government (2021Szvup061), Jiangsu High-Level Innovative and Entrepreneurial Talents Introduction Plan (Shuangchuang Doctor Program, JSSCBS20210166), and a project funded by the Priority Academic Program Development of Jiangsu Higher Education Institutions (PAPD).

AUTHOR DECLARATIONS

Conflict of Interest

There are no conflicts of interest to disclose by the authors that are relevant to the content of this article.

Author Contributions

Zelin Xu: Investigation (equal); Methodology (lead); Writing - original draft (lead); Software (equal). **Kai Fang:** Investigation (equal); Conceptualization (lead); Validation (equal). **Mengran Yu:** Data curation (lead); Validation (equal). **Tiqing Wang:** Software (equal); Visualization (lead). **Peng Li:** Formal analysis (lead); Writing - review & editing (equal). **Zhenghua Qian:** Funding acquisition (lead); Resources (lead); Writing - review & editing (equal). **Dianzi Liu:** Supervision (lead); Project administration (lead).

DATA AVAILABILITY STATEMENT

The data that support the findings of this study are available from the corresponding author upon reasonable request.

Appendix A: Surface potential distribution of the 3D fiber model

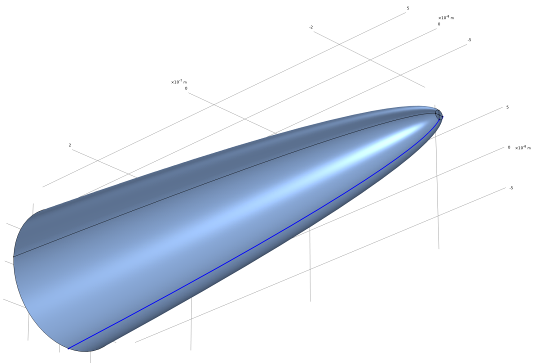

Figure 12: 3D fiber model built in COMSOL

Due to the non-negligible differences in constitutive equations and assumptions between 3D models and 2D models, this section only provides an existence verification. The area function, material and model parameters are the same as in Section V A, with $F = 0.02\ nN$ and $\lambda = 255/256$. The 3D model established using COMSOL software is shown in Figure 12., and the potential distribution on the blue line at the bottom surface is selected to represent the surface potential. The surface potential distribution is shown in Figure 13, where it can be seen that an extremum appears near the right end face of the fiber, verifying the existence of the phenomenon discussed in Section V B and the necessity of related research.

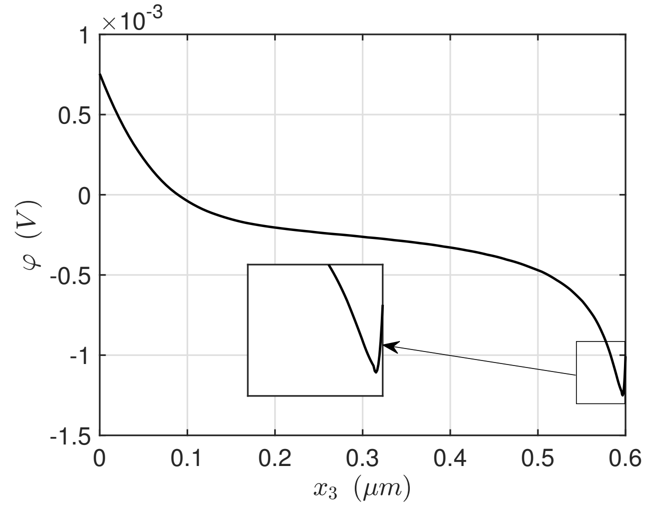

Figure 13: Surface potential distribution of the 3D fiber model

REFERENCES

[1] Y. Qin, X. Wang, and Z. Wang, "Microfibre-nanowire hybrid structure for energy scavenging," Nature **451**, 809–813 (2008).

[2] M. Johar, M. Hassan, A. Waseem, J.-S. Ha, J. Lee, and S.-W. Ryu, "Stable and high piezoelectric output of gan nanowire-based lead-free piezoelectric nanogenerator by suppression of internal screening," Nanomaterials **8** (2018).

[3] X. Wang, J. Zhou, J. Song, J. Liu, N. Xu, and Z. Wang, "Piezoelectric field effect transistor and nanoforce sensor based on a single zno nanowire," Nano Letters **6**, 2768–2772 (2006).

[4] R. Dahiya, G. Metta, M. Valle, A. Adami, and L. Lorenzelli, "Piezoelectric oxide semiconductor field effect transistor touch sensing devices," Applied Physics Letters **95** (2009).

[5] J. Qi, H. Zhang, S. Lu, X. Li, M. Xu, and Y. Zhang, "High performance indium-doped zno gas sensor," Journal of Nanomaterials **2015** (2015).

[6] J. Zhang and J. Zhou, "Humidity-dependent piezopotential properties of zinc oxide nanowires: Insights from atomic-scale modelling," Nano Energy **50**, 298–307 (2018).

[7] W. Wu, Y. Wei, and Z. Wang, "Strain-gated piezotronic logic nanodevices," Advanced Materials **22**, 4711–4715 (2010).

[8] C. Sun, F. Wu, Y. Fu, D. Wallis, R. Mikhaylov, F. Yuan, D. Liang, Z. Xie, H. Wang, R. Tao, M. Shen, J. Yang, W. Xun, Z. Wu, Z. Yang, H. Cang, and X. Yang, "Thin film gallium nitride (gan) based acoustofluidic tweezer: Modelling and microparticle manipulation," Ultrasonics **108** (2020).

[9] C. Pan, J. Zhai, and Z. Wang, "Piezotronics and piezo-phototronics of third generation semiconductor nanowires," Chemical Reviews **119**, 9303–9359 (2019).

[10] G. Wang, J. Liu, X. Liu, W. Feng, and J. Yang, "Extensional vibration

characteristics and screening of polarization charges in a zno piezoelectric semiconductor nanofiber," Journal of Applied Physics **124** (2018).

[11] F. Jiao, P. Wei, X. Zhou, and Y. Zhou, "The dispersion and attenuation of the multi-physical fields coupled waves in a piezoelectric semiconductor," Ultrasonics **92**, 68–78 (2019).

[12] S. Fan, Y. Liang, J. Xie, and Y. Hu, "Exact solutions to the electromechanical quantities inside a statically-bent circular zno nanowire by taking into account both the piezoelectric property and the semiconducting performance: Part i—linearized analysis," Nano Energy **40**, 82–87 (2017).

[13] W. Yang, J. Liu, and Y. Hu, "Mechanical tuning methodology on the barrier configuration near a piezoelectric pn interface and the regulation mechanism on i–v characteristics of the junction," Nano Energy **81** (2021).

[14] R. Cheng, C. Zhang, W. Chen, and J. Yang, "Piezotronic effects in the extension of a composite fiber of piezoelectric dielectrics and nonpiezoelectric semiconductors," Journal of Applied Physics **124** (2018).

[15] Y. Qu, F. Jin, and J. Yang, "Torsion of a flexoelectric semiconductor rod with a rectangular cross section," Archive of Applied Mechanics **91**, 2027–2038 (2021).

[16] Y. Hu, Y. Zhang, C. Xu, G. Zhu, and Z. Wang, "High-output nanogenerator by rational unipolar assembly of conical nanowires and its application for driving a small liquid crystal display," Nano Letters **10**, 5025–5031 (2010).

[17] R. Araneo, G. Lovat, P. Burghignoli, and C. Falconi, "Piezo-semiconductive quasi-1d nanodevices with or without anti-symmetry," Advanced Materials **24**, 4719–4724 (2012).

[18] R. Araneo and C. Falconi, "Lateral bending of tapered piezo-semiconductive nanostructures for ultra-sensitive mechanical force to voltage conversion," Nanotechnology **24** (2013).

[19] K. Fang, P. Li, N. Li, D. Liu, Z. Qian, V. Kolesov, and I. Kuznetsova, "Model and performance analysis of non-uniform piezoelectric semiconductor nanofibers," Applied Mathematical Modelling **104**, 628–643 (2022).

[20] C. Ren, K. Wang, and B. Wang, "Adjusting the electromechanical coupling behaviors of piezoelectric semiconductor nanowires via strain gradient and flexoelectric effects," Journal of Applied Physics **128** (2020).

[21] R. F. Pierret and G. W. Neudeck, *Advanced semiconductor fundamentals*, Vol. 6 (Addison-Wesley Reading, MA, Boston, 1987).

[22] A. Hutson and D. White, "Elastic wave propagation in piezoelectric semiconductors," Journal of Applied Physics **33**, 40–47 (1962).

[23] B. Auld, "Application of microwave concepts to the theory of acoustic fields and waves in solids," IEEE Transactions on Microwave Theory and Techniques **17**, 800–811 (1969).

[24] X. Dai, Z. Qian, and J. Yang, "A semi-analytical solution for electric double layers near an elliptical cylinder," Acta Mechanica Sinica/Lixue Xuebao **34**, 62–67 (2018).

[25] Y. Liang and Y. Hu, "Effect of interaction among the three time scales on the propagation characteristics of coupled waves in a piezoelectric semiconductor rod," Nano Energy **68** (2020).

[26] K. Fang, P. Li, and Z. Qian, "Static and dynamic analysis of a piezoelectric semiconductor cantilever under consideration of flexoelectricity and strain gradient elasticity," Acta Mechanica Solida Sinica **34**, 673–686 (2021).

[27] Y. Qu, F. Jin, and J. Yang, "Effects of mechanical fields on mobile charges in a composite beam of flexoelectric dielectrics and semiconductors," Journal of Applied Physics **127**, 194502 (2020).

[28] Y. Luo, C. Zhang, W. Chen, and J. Yang, "Piezopotential in a bended composite fiber made of a semiconductive core and of two piezoelectric layers with opposite polarities," Nano Energy **54**, 341–348 (2018).

[29] N. Li, Z. Qian, and J. Yang, "Effects of edge and interior stresses on electrical behaviors of piezoelectric semiconductor films," Ferroelectrics **571**, 96–108 (2021).

[30] Y. Qu, F. Jin, and J. Yang, "Temperature-induced potential barriers in piezoelectric semiconductor films through pyroelectric and thermoelastic couplings and their effects on currents," Journal of Applied Physics **131** (2022).

[31] M. Li, Q. Zhang, B. Wang, and M. Zhao, "Analysis of flexural vibrations of a piezoelectric semiconductor nanoplate driven by a time-harmonic force," Materials **14** (2021).

[32] Y. Luo, C. Zhang, W. Chen, and J. Yang, "Piezotronic effect of a thin film with elastic and piezoelectric semiconductor layers under a static flexural loading," Journal of Applied Mechanics, Transactions ASME **86** (2019).

[33] R. Tian, J. Liu, E. Pan, Y. Wang, and A. Soh, "Some characteristics of elastic waves in a piezoelectric semiconductor plate," Journal of Applied Physics **126** (2019).

[34] Z. Yang, Z. Zhang, C. Liu, C. Gao, W. Chen, and C. Zhang, "Analysis of a hollow piezoelectric semiconductor composite cylinder under a thermal loading," Mechanics of Advanced Materials and Structures (2022).

[35] Z. Yang, L. Sun, C. Zhang, C. Zhang, and C. Gao, "Analysis of a composite piezoelectric semiconductor cylindrical shell under the thermal loading," Mechanics of Materials **164** (2022).

[36] X. Guo and P. Wei, "Dispersion relations of in-plane elastic waves in nanoscale one dimensional piezoelectric semiconductor/piezoelectric dielectric phononic crystal with the consideration of interface effect," Applied Mathematical Modelling **96**, 189–214 (2021).

[37] R. Tian, G. Nie, J. Liu, E. Pan, and Y. Wang, "On rayleigh waves in a piezoelectric semiconductor thin film over an elastic half-space," International Journal of Mechanical Sciences **204** (2021).

[38] J. He, J. Du, and J. Yang, "Stress effects on electric currents in antiplane problems of piezoelectric semiconductors over a rectangular domain," Acta Mechanica **233**, 1173–1185 (2022).

[39] R. Mindlin, "Low frequency vibrations of elastic bars," International Journal of Solids and Structures **12**, 27–49 (1976).

[40] M. Dökmeci, "A theory of high frequency vibrations of piezoelectric cyrstal bars," International Journal of Solids and Structures **10**, 401–409 (1974).

[41] J. Yang, "Equations for the extension and flexure of a piezoelectric beam with rectangular cross section and applications," International Journal of Applied Electromagnetics and Mechanics **9**, 409–420 (1998).

[42] C. Shu, *Differential quadrature and its application in engineering* (Springer Science & Business Media, New York, 2012).

[43] R. Bellman and J. Casti, "Differential quadrature and long-term integration," Journal of Mathematical Analysis and Applications **34**, 235–238 (1971).

[44] K. Wang and B. Wang, "Electrostatic potential in a bent piezoelectric nanowire with consideration of size-dependent piezoelectricity and semiconducting characterization," Nanotechnology **29** (2018).

[45] C. Zhang, X. Wang, W. Chen, and J. Yang, "Bending of a cantilever piezoelectric semiconductor fiber under an end force," Advanced Structured Materials **90**, 261–278 (2018).